

DISENTANGLING 3D ANIMAL POSE DYNAMICS WITH SCRUBBED CONDITIONAL LATENT VARIABLES

Anonymous authors

Paper under double-blind review

ABSTRACT

Methods for tracking lab animal movements in unconstrained environments have become increasingly common and powerful tools for neuroscience. The prevailing hypothesis is that animal behavior in these environments comprises sequences of discrete stereotyped body movements ("motifs" or "actions"). However, the same action can occur at different speeds or heading directions, and the same action may manifest slightly differently across subjects due to, for example, variation in body size. These and other forms of nuisance variability complicate attempts to quantify animal behavior in terms of discrete action sequences and draw meaningful comparisons across individual subjects. To address this, we present a framework for motion analysis that uses conditional variational autoencoders in conjunction with adversarial learning paradigms to disentangle behavioral factors. We demonstrate the utility of this approach in downstream tasks such as clustering, decodability, and motion synthesis. Further, we apply our technique to improve disease detection in a Parkinsonian mouse model.

1 INTRODUCTION

Animal behavior is largely expressed through movement (Musall et al., 2019; Bernstein, 1967). Thus, the ability to identify changes in animal movement is critical for understanding neural (dys)function (McCullough & Goodhill, 2021). In recent years, pose estimation has become popular for behavioral measurement (Dunn et al., 2021; Nath et al., 2019; Zimmermann et al., 2020; Bala et al., 2020; Pereira et al., 2022), enabling more objective and comprehensive kinematic profiling. Given the increasing throughput and dimensionality of behavioral measurement assays (Nourizonoz et al., 2020; Bialek, 2022; Marshall et al., 2022), the ability to learn meaningful and interpretable representations of behavior is essential (Datta et al., 2019).

A common analysis goal is to cluster or segment recurring and stereotyped pose sequences—such as running, turning, and rearing—and compare their frequencies and transition statistics across experimental conditions (Berman et al., 2014; Weinreb et al., 2023; Wiltshko et al., 2020; 2015b; Marshall et al., 2022). Currently, most approaches are purely unsupervised and can be sensitive to nuisance variability, such as animal individuality, or over-segment due to continuous variability, such as speed (Van Dam et al., 2023; Costacurta et al., 2022). As a result, these methods often produce action spaces in which true biological signals are uninterpretablely entangled with confounding variables or uninformative features. For example, the same fundamental action (e.g. walking) can be performed with different levels of vigor (fast vs. slow) and with different directionality (walking straight vs. slightly turning left or right). All of these variants are typically split into different action clusters (see Marshall et al., 2022), introducing extraneous statistical structure that may obscure more meaningful biological signals.

In principle, action spaces could be made invariant to nuisance variables via disentanglement of specified factors (Shu et al., 2019), thus permitting the identification and analysis of meaningful behavioral dynamics (Shi et al., 2021; Whiteway et al., 2021; Yi & Saxena, 2022). However, existing disentanglement approaches have shortcomings. The increasingly common conditional variational autoencoder (C-VAE) approach learns accurate disentangled representations of the conditional variable, such that changing it while holding the other latent variables fixed generates outputs varying only in the conditional factor (Petrovich et al., 2021b; Guo et al., 2020; Khemakhem et al., 2020). However, we will show that the other latent variables are not necessarily, nor typically, invariant

to the conditional factor. Adversarial approaches can be used to learn disentangled subspaces with specific invariances (Ding et al., 2020; Sanchez et al., 2020; Zhao et al., 2021; Brakel & Bengio, 2017), but these methods rely on secondary neural networks that can be difficult to train and sensitive to architectural and hyperparameter choices (Arjovsky & Bottou, 2017; Radford, 2015). Furthermore, adversarial neural networks often target fully disentangled representations, e.g., via mutual information minimization (Belghazi et al., 2018; Cheng et al., 2020), but certain nuisance variables, like speed, have *some* dependencies with action understanding (e.g. a subject will always move farther during locomotion than when grooming). Fully disentangling such variables into invariant subspaces would destroy relevant behavioral variation. Ideally, the degree of disentanglement could be easily specified and controlled.

To address these challenges, we present scrubbed C-VAEs (SC-VAE) for learning disentangled motion features from 3D pose sequences (Fig. 1a). Given a variable to disentangle (calculated deterministically or known *a priori*), SC-VAE seeks to learn a latent representation in which the variable cannot be decoded by specified linear or nonlinear functions, called "scrubbers". SC-VAE achieves this by conditioning a VAE on disentanglement variables while adversarially penalizing the encoder based on a scrubber’s ability to estimate variable information from the latent representation. As a result, we obtain a variational distribution with direct control over the level of contribution from nuisance variability (Fig. 1b).

We show that scrubbing enhances latent representations by encouraging nuisance-invariant clusters and improving the consistency of the conditional generative model. We also demonstrate SC-VAE’s ability to enhance and disentangle biological phenotypes from nuisance factors in a mouse model of Parkinson’s disease, illustrating how SC-VAE can be used to further neurobehavioral inquiry. When examining different choices of scrubbing, we find that: 1) neural network scrubbers built from existing adversarial disentanglement methods are less reliable than scrubbers with explicit parametric assumptions, and 2) assumptions of linear or nonlinear disentanglement can impact downstream analyses due to the level of dependence between disentangled variables and behavioral understanding.

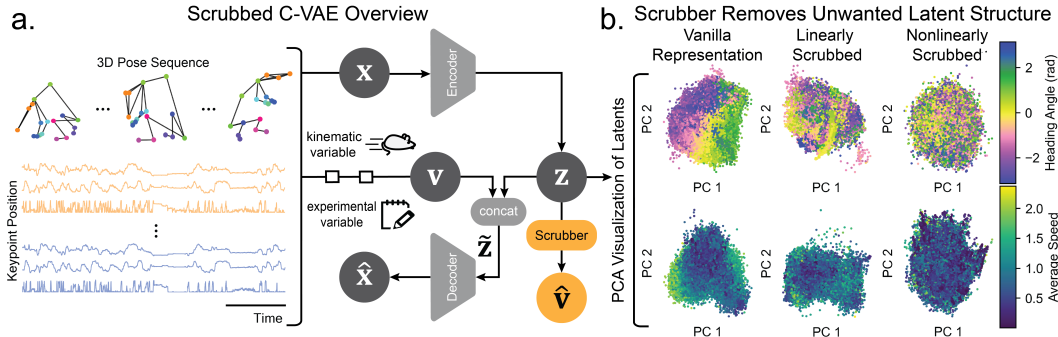


Figure 1: **Overview of SC-VAE.** (a) SC-VAE encourages disentangled representations by directly concatenating known factors to latent variables in a conditional VAE. (b) A "scrubber" removes information about these factors from the latent variables, such that factors are unable to be explained by specified linear or nonlinear functions.

2 PRIOR WORK

Models of animal movement Finescale manual annotation (e.g., rears, turns) of animal behaviors is time-intensive and subjective. Further, many experimental manipulations—such as new pharmacological treatments—induce unknown behavioral phenotypes (Nestler & Hyman, 2010). Thus, most research has gravitated towards unsupervised, data-driven methods. Popular approaches apply dimensionality reduction and clustering to wavelet-transformed pose sequences (Berman et al., 2014; Marshall et al., 2021) or auto-regressive hidden Markov models (ARHMMs) to model action motifs as discrete states with intra-state linear dynamics (Wiltchko et al., 2015a; Weinreb et al., 2023).

More recently, deep neural networks have been leveraged to learn low-dimensional representations of behavior. Due to challenging perspective and illumination effects in videos, many behavioral analysis methods use pose trajectories—and increasingly 3D poses (Marshall et al., 2022)—as input

(Dunn et al., 2021; Nath et al., 2019; Zimmermann et al., 2020; Bala et al., 2020; Pereira et al., 2022). For example, VAME generates single-frame pose embeddings from variational autoencoders as a nonlinear feature learning step before fitting an ARHMM (Luxem et al., 2022). BAMS, on the other hand, generates representations by predicting distributions of future kinematics (Azabou et al., 2024).

Our study builds on these works by applying constraints on representational spaces to reduce the contribution of nuisance effects and provide control over these behavioral representations. Our motivation is perhaps most similar to previous work by Costacurta et al. (2022), who developed time-warped extensions to the ARHMM to separate changes in speed from other behavioral factors. Despite similar motivations, our method aims to be a more general tool for disentanglement which learns low-dimensional feature spaces robust to a wider range of factors and that could be used for additional tasks beyond time series clustering.

Disentangled representations Although deep networks have the capacity to capture complex nonlinear dynamics, the feature spaces identified by deep networks are not always immediately interpretable and prone to learning undesirable representations due to dataset-specific idiosyncrasies. This unpredictability in learning deep representations has limited their use in the exploratory manner required by experimental research (von Ziegler et al., 2021).

A broad literature on the use of deep networks to extract *disentangled* representations of complex, high-dimensional datasets seeks to address these challenges (Gilpin et al., 2018). While many have investigated the possibility of fully unsupervised disentanglement with VAE-like architectures (e.g., β -VAE and its variants) (Higgins et al., 2017; Chen et al., 2018; Esmaili et al., 2019), doing so is challenging in practice. Further assumptions are usually needed to theoretically guarantee identifiability and disentanglement (Locatello et al., 2019), leading to increasing popularity in weakly supervised disentanglement (Shu et al., 2019; Khemakhem et al., 2020).

Neuroscientists have applied and adapted ideas from this literature to account for nuisance variability in raw video data, such as changes in illumination or slight differences in camera angles over days (Whiteway et al., 2021; Shi et al., 2021; Yi & Saxena, 2022). Here we focus on 3D pose data and aim to disentangle additional forms of nuisance variation such as speed and angular heading, which are cheaply computable from the inferred pose tracks, and animal identity (a type of batch effect). While we focus on these specific variables here, our approach should generalize to other nuisance factors in the future. Prior neuroscience applications of disentanglement have shown success in identifying subspaces for factors. However, they have not explored the invariance over those factors in opposing subspaces.

Our approach is in line with the formalization of disentanglement by Shu et al. (2019) as *both* the ability of: 1) a disentangled dimension to accurately represent a factor, and 2) the corresponding null space to be invariant to that factor. Although there exist disentanglement methods in other application fields that apply both properties (Zhao et al., 2021; Sanchez et al., 2020; Ding et al., 2020), these methods rely on the specification of secondary networks to remove residual factor information in a representation space, often via adversarial training (Ganin & Lempitsky, 2015b; Brakel & Bengio, 2017; Cheng et al., 2020). Here, we contribute novel strategies that: 1) bypass the need for specifying architectures or hyperparameters for adversarial networks, and 2) are more specific about the degree of disentanglement when variables are not perfectly independent of behavioral understanding.

3 METHODS

3.1 POSE PREPROCESSING

We apply our method to 3D body pose sequences extracted from raw videos. This preprocessing step removes several confounding variables such as differences in illumination across recording sessions. However, some residual sources of variability remain, such as differences in body size across subjects. Typical methods of pose preprocessing involve translating and rotating all postures to a root position and direction (i.e., "pointing north") (Marshall et al., 2021; Luxem et al., 2022). However, important trajectory and turning information are lost when this alignment is performed on each frame independently. To avoid this loss of information, we apply a single rotation and translation to all frames in a pose sequence to align the pose at a central time point. That is, given a window of time around a central reference frame, we translate and rotate each posture such that the central

frame is at a specified position and orientation (Fig. 4). In a subset of experiments, we refrained from rotating the pose entirely to demonstrate the ability of our method to disentangle the heading direction and recapitulate a representation commensurate with the fully processed data.

In contrast to some existing methods (e.g. Luxem et al., 2022), we represent pose using joint angles between keypoints positioned at fixed distances from their neighbors. Intuitively, this representation forces any pose dynamics model to obey the physical constraints of the body skeleton, leading to cleaner generative samples (see discussion in Marshall et al., 2021; Huang et al., 2017; Vemulapalli et al., 2014). Optimizing over raw angular variables is complicated by discontinuities; thus we follow a well-established protocol from the computer vision community for lifting 3D rotation matrices into a continuous 6D space (Zhou et al., 2019). Each posture composed of K joint angles is then represented as a $(6K + 3)$ -dimensional vector, where the three additional dimensions come from the global position of the root keypoint. Altogether, each pose sequence is denoted $\mathbf{x}_t \in \mathbb{R}^{L \times (6K + 3)}$ for a sequence over L frames centered at frame t .

3.2 DISENTANGLED REPRESENTATIONS AND CONDITIONAL VAE ARCHITECTURE

Disentangled variables Our core goal is to learn a low-dimensional representation of behavior where simple factors—e.g., speed, heading direction, and animal identity—are put into orthogonal dimensions from factors that are learned in a data-driven, unsupervised fashion. In essence, this would separate the semantic content of actions—whether the animal is running, digging, rearing, etc.—from the character of these actions—whether the animal is running fast vs. slow or oriented differently when turning.

We formalize this goal as follows. We assume that for any pose sequence \mathbf{x}_t we can compute a vector of nuisance factors $\mathbf{v}_t \in \mathbb{R}^N$ (e.g. speed or heading direction). Loosely, we will say that a latent representation $\tilde{\mathbf{z}}_t$ taking values in \mathbb{R}^D is *disentangled* with respect to \mathbf{v}_t when one can identify two orthogonal subspaces \mathbf{z}_t and \mathbf{z}'_t such that \mathbf{v}_t can be reliably inferred from \mathbf{z}'_t but not reliably inferred from \mathbf{z}_t . In other words, the goal is to have \mathbf{z}'_t capture known behavioral factors, while \mathbf{z}_t reflects unknown behavioral factors that are learned from the data with minimal redundancies to \mathbf{z}'_t .

Variational autoencoders (VAEs) The backbone of our method is a VAE with 1D convolutional layers (Kingma & Welling, 2013). Adopting standard notation, we use an encoder network q_ϕ to map pose sequences onto a distribution over latent variables sampled via a reparameterization trick, $\mathbf{z}_t \sim q_\phi(\cdot | \mathbf{x}_t)$. The pose sequence is then reconstructed by a decoding network which evaluates the likelihood $p_\theta(\mathbf{x} | \mathbf{z}_t)$. In a standard VAE, the parameters $\{\phi, \theta\}$ are adjusted with respect to the evidence lower bound (ELBO):

$$L_{\text{ELBO}}(\phi, \theta) = -\mathbb{E}_{\mathbf{x}_t} [\mathbb{E}_{\mathbf{z}_t \sim q_\phi(\cdot | \mathbf{x}_t)} [\log p_\theta(\mathbf{x}_t, \mathbf{z}_t) - \log q_\phi(\mathbf{z}_t | \mathbf{x}_t)]] \quad (1)$$

Conditional VAEs (C-VAEs) An established way to promote disentanglement in a supervised fashion is to use a conditional VAE (Sohn et al., 2015; Khemakhem et al., 2020). C-VAEs are a popular approach for controllable human motion synthesis, as they can generate realistic body pose sequences that correspond to categorical actions (e.g. throwing, kicking, or lunging, Guo et al., 2020; Petrovich et al., 2021a; Gu et al., 2024). C-VAEs have also been exploited within neuroscience (Wu et al., 2020), but to our knowledge, have not been leveraged for behavioral representation learning.

Here, latent variables are sampled from a conditional prior distribution that depends on another variable, \mathbf{v}_t , which is observed separately or derived deterministically from \mathbf{x}_t . In our case, \mathbf{v}_t will correspond to a vector representation of the animal’s running speed, heading direction, or one hot encoding of the animal’s identity. Exact implementations for C-VAEs vary. We choose a simple approach of concatenating \mathbf{v}_t onto the sampled output of the encoder network. That is, we sample $\mathbf{z}_t \sim q_\phi(\cdot | \mathbf{x}_t)$ while \mathbf{z}'_t is strictly defined by \mathbf{v}_t . A new vector $\tilde{\mathbf{z}}_t = [\mathbf{z}_t \ \mathbf{v}_t]^\top$ is passed to the decoding network. A C-VAE is then trained with respect to the same ELBO loss, which is now interpreted as a lower bound of the expected conditional marginal likelihood, conditioning with respect to \mathbf{v}_t . For full details on model architectures, see C.1.

Intuitively, since \mathbf{z}_t and \mathbf{v}_t are both passed to the decoder, any information about \mathbf{v}_t that is encoded by \mathbf{z}_t is redundant and inefficient. Thus, if the latent dimension D is small, one expects that the C-VAE will learn a disentangled representation. While this intuition is borne out to a certain extent in practice, our experience (documented below in Sec. 4) shows that a C-VAE will often learn a distribution over

\mathbf{z}_t that is only partly disentangled from \mathbf{v}_t . Further, choosing a smaller latent dimension D can be expected to result in more disentanglement, but less expressivity and trainability. Thus, a vanilla C-VAE seems to impose an unfortunate trade-off between faithful modeling of the data and learning disentangled latents.

3.3 SCRUBBING OUT RESIDUAL INFORMATION

A core component of our approach is to augment the C-VAE loss function to reduce dependence between \mathbf{z}_t and \mathbf{v}_t . This is analogous to minimizing mutual information (MI), $I(\mathbf{v}_t, \mathbf{z}_t) = \mathbb{E}_{\mathbf{v}_t, \mathbf{z}_t} [\log(p(\mathbf{v}_t, \mathbf{z}_t)/p(\mathbf{v}_t)p(\mathbf{z}_t))]$. Although MI maximization is commonly used to generate representations with shared features between paired samples (Hjelm et al., 2018; Bachman et al., 2019; Zhao et al., 2021; Sanchez et al., 2020), there are generally no tractable upper bounds for minimization (Poole et al., 2019). In the context of behavioral analysis, our objective is to create a representation space in which \mathbf{v}_t is "hidden" from downstream analyses with constrained expressiveness (e.g. linear regression or clustering via a Gaussian mixture model). We therefore substitute MI with predictive information (Xu et al., 2020b):

$$I_f(\mathbf{v}_t, \mathbf{z}_t) = \max_{\psi} [\mathbb{E}_{\mathbf{x}_t, \mathbf{v}_t} [\mathbb{E}_{\mathbf{z}_t \sim q_{\phi}(\cdot | \mathbf{x}_t)} [\log p(\mathbf{v}_t | f_{\psi}(\mathbf{z}_t))]]] \quad (2)$$

where $f_{\psi}(\cdot)$ is a potentially nonlinear function family parameterized by ψ , and $\log p(\mathbf{v}_t | f_{\psi}(\mathbf{z}_t))$ is the log-likelihood of \mathbf{v}_t conditioned on sufficient statistics $f_{\psi}(\mathbf{z}_t)$. Given an approximate maximizer $\hat{\psi}$ of eq. (2), we promote disentanglement by introducing the adversarial penalty, $L_{\text{scrub}}(\phi) = \hat{I}_f(\mathbf{v}_t, \mathbf{z}_t)$. We then seek to jointly minimize $L_{\text{ELBO}}(\phi, \theta) + \lambda L_{\text{scrub}}(\phi)$ over the model parameters $\{\phi, \theta\}$ for some user-specified hyperparameter $\lambda > 0$.

Thus, $f_{\psi}(\cdot)$ is an adversarial decoder that aims to maximize the log-likelihood of \mathbf{v}_t given \mathbf{z}_t . This penalty term is minimized when the encoder network, parameterized by ϕ , encodes a variational distribution over \mathbf{z}_t with no decodable information about \mathbf{v}_t . This would imply perfect disentanglement with respect to the class of functions parameterized by ψ . Mutual information is recovered in the limit that $f_{\psi}(\cdot)$ defines an arbitrarily complex probability density (see Xu et al., 2020b), but we will see that it can be advantageous to constrain $f_{\psi}(\cdot)$ to a more limited class of functions (e.g., linear or low-order polynomial).

The effect of the penalty term λL_{scrub} is to "scrub out" information about \mathbf{v}_t contained in \mathbf{z}_t , and we therefore call $f_{\psi}(\cdot)$ a "scrubber." The overall model architecture is diagrammed in Fig. 1A. However, it is challenging to efficiently solve the inner maximization problem over ψ in eq. (2). We now describe several strategies to overcome this challenge.

3.4 SCRUBBING WITH ADVERSARIAL NEURAL NETWORKS

A classic approach to adversarial training is to define f_{ψ} to be a neural network trained jointly with the C-VAE. We implement two such methods here for disentangling behavioral representations.

Scrubbing with gradient reversal layers (SC-VAE-GR) First, we apply an existing method that is popular in the context of domain adaption in deep networks (Ganin & Lempitsky, 2015a) and applied to disentanglement (Ding et al., 2020). Where f_{ψ} is a multi-layer perception (MLP) ensemble, the idea is to estimate the gradient of:

$$\mathbb{E}_{\mathbf{x}_t, \mathbf{v}_t} [\mathbb{E}_{\mathbf{z}_t \sim q_{\phi}(\cdot | \mathbf{x}_t)} [\log p(\mathbf{v}_t | f_{\psi}(\mathbf{z}_t))]] \quad (3)$$

with respect to ψ and ϕ over a minibatch of pose sequences. Then, we simultaneously perform gradient ascent and descent updates on ψ and ϕ , respectively. This is akin to jointly training the model over $\{\psi, \phi, \theta\}$ but with the gradients reversed for ψ .

Scrubbing with neural discriminators (SC-VAE-ND) An alternative approach investigated by Sanchez et al. (2020), Brakel & Bengio (2017), and Kim & Mnih (2018) draws inspiration from generative adversarial networks (GANs; Goodfellow et al., 2020). Given a latent sample $[\mathbf{z}_i \quad \mathbf{v}_i]^{\top}$, we generate a "fake" sample $[\mathbf{z}_i \quad \mathbf{v}_{j \neq i}]^{\top}$ and define an adversarial discriminator, f_{ψ} , to classify real from fake representations. By minimizing the cross-entropy loss of this classifier, the mutual information between \mathbf{z}_t and \mathbf{v}_t is minimized (Brakel & Bengio, 2017). Unlike for the rest of the methods in this paper, \hat{f}_{ψ} and the C-VAE are trained in alternation for SC-VAE-ND.

Challenges These strategies can work if one carefully tunes separate learning rates for ψ and $\{\phi, \theta\}$. However, we found that fine-tuning these hyperparameters was, perhaps unsurprisingly, challenging in practice (Shen et al., 2020; Scaramuzzino et al., 2023). When not delicately tuned, $\hat{\psi}$ fails to track the distribution of \mathbf{z}_t induced by parameter updates to the encoder q_ϕ . Thus, $\hat{f}_\psi(\cdot)$ will be a suboptimal adversary, and $\hat{I}_f(\cdot)$ will not be tight to $I_f(\cdot)$. Furthermore, these approaches have strong assumptions of nonlinear disentanglement which may not be appropriate in cases where the scrubbed variable is not independent (see Sec. 4.2 and 4.4). In the following methods, we navigate these challenges by: 1) adaptively tuning learning rates, 2) applying more direct estimations of ψ or $I_f(\cdot)$ which do not require specifying network architectures or their hyperparameters, and 3) introducing scrubbers with more constrained (e.g., linear or quadratic) assumptions of scrubbing.

3.5 SCRUBBING UNDER PARAMETRIC CONSTRAINTS

Linear scrubbing by moving average least squares (SC-VAE-MALS) If we constrain $f_\psi(\mathbf{z}_t)$ to be a linear function and use a Gaussian likelihood to model \mathbf{v}_t , then the maximization over ψ is simply an ordinary least squares problem. The optimal prediction can be calculated in closed-form by the normal equations (see e.g., Murphy, 2012, Ch. 7):

$$f_\psi(\mathbf{z}_t) = \mathbb{E}[\mathbf{v}\mathbf{z}^\top] (\mathbb{E}[\mathbf{z}\mathbf{z}^\top] + \beta\mathbf{I})^{-1} \mathbf{z}_t \quad (4)$$

where β is the L2-regularization constant. Thus, to evaluate $L_{\text{scrub}}(\phi)$ for a linear model, we simply need to keep a running estimate of two matrices: $\psi^0 = \mathbb{E}[\mathbf{v}\mathbf{z}^\top]$ and $\psi^1 = \mathbb{E}[\mathbf{z}\mathbf{z}^\top]$. We do this by computing exponential moving averages (EMA) of these quantities, replacing expectations with empirical averages. Given a single data instance, \mathbf{x}_t , we sample $\mathbf{v}_t, \mathbf{z}_t \sim q_\phi(\cdot | \mathbf{x}_t)$, and update our estimate of the sufficient statistics accordingly:

$$\hat{\psi}^0 \leftarrow [(1 - \alpha)\mathbf{v}_t\mathbf{z}_t^\top + \alpha\hat{\psi}^0] \quad (5)$$

$$\hat{\psi}^1 \leftarrow [(1 - \alpha)\mathbf{z}_t\mathbf{z}_t^\top + \alpha\hat{\psi}^1] \quad (6)$$

where α is the smoothing factor of this EMA filter. In practice, we compute these updates over a minibatch with multiple data samples. We forgo manual tuning of α by running two EMA filters in parallel with separate smoothing factors at a small, fixed difference. On each minibatch, we increment or decrement the smoothing factors based on which filter provides a better fit to the minibatch statistics (see A.2 for details).

Extension to scrubbing by polynomial regression The method above immediately extends to polynomial regression by augmenting \mathbf{z}_t to include higher-order polynomial features to obtain quadratic (-MAQS) and cubic (-MACS) scrubbing. This enables progressive nonlinear scrubbing.

Categorical scrubbing with adaptive quadratic discriminators (SC-VAE-QD) The EMA filter can also be readily applied to other scrubbing models beyond ordinary least squares. When \mathbf{v}_t is a categorical variable encoding animal identity, we treat $f_\psi(\mathbf{z}_t)$ as a prediction of the class label. A simple approach is to keep a running estimate of the class-conditional means, $\mathbb{E}_{\mathbf{v}=c}[\mathbf{z}]$, and covariances, $\text{Cov}_{\mathbf{v}=c}[\mathbf{z}, \mathbf{z}]$, and then use a quadratic discriminant analysis (QDA) classifier $\hat{f}_\psi(\mathbf{z}) = \hat{p}(\mathbf{v}_t = c | \mathbf{z}_t)$ (see A.2). We update the mean and covariance estimates in the same way as eq. (5) and eq. (6) with the self-tuning smoothing factor.

Nonlinear scrubbing with kernel density mutual information estimators (SC-VAE-MI) The constrained adversarial maximization over $f_\psi(\cdot)$ is related to classical quantities in information theory. In particular, if the class of functions parameterized by ψ contains all possible models, then minimizing $L_{\text{scrub}}(\phi)$ is equivalent to minimizing the mutual information between \mathbf{v}_t and \mathbf{z}_t (Xu et al., 2020a). Above, we built scrubbers assuming a parametric form for $f_\psi(\cdot)$ (e.g. linear or quadratic), but we can also develop a scrubber that estimates the mutual information in a nonparametric fashion. We investigated a simple approach of using Gaussian kernel density estimation to approximate the joint probability density $\hat{p}(\mathbf{v}_t, \mathbf{z}_t)$. Given this approximation of the density, $\hat{I}(\mathbf{v}_t, \mathbf{z}_t) = \mathbb{E}_{\mathbf{v}_t, \mathbf{z}_t} [\log(\hat{p}(\mathbf{v}_t, \mathbf{z}_t) / \hat{p}(\mathbf{v}_t)\hat{p}(\mathbf{z}_t))]$ provides an estimate of the mutual information (Moon et al., 1995). It is well-known that mutual information estimators suffer a curse of dimensionality; to combat this, we use a large batch size (2048 pose sequences) and tune the bandwidth parameter of the Gaussian kernel to compromise between estimator bias and variance. This results in a biased estimate of mutual information, which we identify with $L_{\text{scrub}}(\phi)$.

4 RESULTS

4.1 DATA

We used data from $n = 3$ C57BL/6 mice freely exploring a 30 cm² open field (324k frames per mouse, 1 hour at 90 fps). For applications, we used $n = 36$ C57BL/6 mice recorded in 1-hour sessions (90 fps) in this same open field before and after Parkinson’s disease (PD) induction (6-OHDA unilateral injection model). 3D poses were tracked with DANNCE (Dunn et al., 2021). In each animal, we also performed fluorescent immunostaining of the striatum bilaterally and quantified the extent of dopaminergic neurodegeneration as the ratio of integrated fluorescence between the lesioned to non-lesioned hemisphere (more details in D).

4.2 DISENTANGLING NUISANCE VARIABLES

For all results, we trained separate models to isolate the effects of each scrubber on each nuisance variable. For implementation details, see B and C.

Heading direction We first tested heading direction disentanglement in models trained *without* rotationally processed data as described in Section 3.1. As the optimal representation can be derived by fitting a VAE to fully processed pose sequences (VAE Processed), heading disentanglement serves as an ideal baseline to validate our scrubbing methods. When examining a vanilla VAE trained on raw (not rotationally-processed) data, heading direction was, unsurprisingly, linearly decodable from the latents (Fig. 2a). Conditioning the latent variable was not sufficient to disentangle heading direction from other latent factors; a C-VAE conditioned on heading direction formed representations that were structured with heading direction in a similar way to the vanilla VAE, despite being redundant with the conditioned variable. Although SC-VAE-GR and -ND use nonlinear adversaries (i.e., an MLP), we found they were unreliable in producing representations that were even linearly invariant to heading. SC-VAE-MALS was found to be more reliable in achieving linear disentanglement by directly estimating a linear adversary.

Although SC-VAE-MALS was successful in linear disentanglement, an optimal representation arguably should have near complete disentanglement (beyond linear) of heading direction, since the facing direction of a behavior does not affect its semantic label.¹ Scrubbing by quadratic regression (SC-VAE-MAQS) or mutual information estimation (SC-VAE-MI) reached nonlinear decodability commensurate with the rotationally preprocessed optimum (VAE Processed). Thus, both SC-VAE-MI and -MAQS exhibit strong linear and nonlinear disentanglement. We then tested SC-VAE disentanglement on speed and animal identity, nuisance variables whose influences on behavioral representations cannot be trivially removed via data preprocessing.

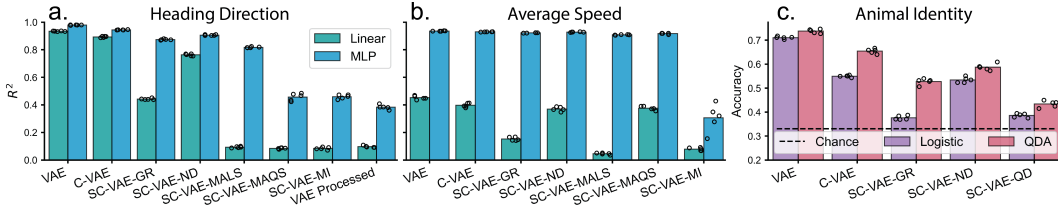


Figure 2: **Decoding nuisance variables from scrubbed latents.** R^2 for linear and nonlinear (MLP) regression on (a) speed and (b) heading from latents. (c) Classification accuracy for animal identity using logistic regression and quadratic discriminants.

Speed Unlike with heading direction, speed is naturally entangled with behavioral factors—e.g., rearing and running exhibit inherently different speed profiles. The generative model defined by the VAE ought to reflect this dependence, so some nonlinear dependence between speed and the unsupervised latents ought to be preserved and not "scrubbed out". On the other hand, the same

¹Importantly, we will argue below that this logic does not apply to some other behavioral variables, such as the animal’s speed, which are *not* independent of action categories. In these cases, fully nonlinear scrubbing may lead to undesirable performance but a constrained (e.g., linear) scrubber can provide partial disentanglement.

action can be performed at different speeds, so it would be desirable to at least partially disentangle speed from other variables. Trends for linear and nonlinear disentanglement across models for speed scrubbing were similar to our heading results (Fig. 2b). SC-VAE-MAQS was the exception where it did not affect speed disentanglement. Although SC-VAE-MI continued to exhibit strong disentanglement, this came at the expense of having interpretable clusters of actions within the latent space. We further explore the subtleties of linear vs nonlinear speed disentanglement in Section 4.4.

Animal identity Small differences in subject limb proportions or sizes can affect behavioral kinematics and postures in complex nonlinear ways, even in pose preprocessing without explicit notions of limb lengths (e.g., ours described in Sec. 3.1). These differences cause trivial separations of the same behaviors across individuals. When scrubbing animal identity, SC-VAE representations were also the most linearly and nonlinearly invariant, with classification from SC-VAE-GR and SC-VAE-QD latents approaching chance accuracy using linear decision boundaries (Fig. 2c). Like with heading direction and speed, gradient reversal (SC-VAE-GR) was less effective than using a specified nonlinear scrubber (SC-VAE-QD) for nonlinear identity disentanglement.

Scrubbing effects were evident when visualizing latent representations (Fig. 1b, 6). Vanilla VAE and C-VAE representations were highly entangled with nuisance variables across principal axes, with regions dominated by specific speeds, heading directions, or animal identities. The scrubbing models showed representations with more mixing across nuisance variables. SC-VAE-MI, for heading and speed, and SC-VAE-QD, for identity, produced the most "salt and pepper" representations.

Table 1: **Effects of scrubbing on motion synthesis.** R^2 of heading or speed of generated behaviors with respect to random heading or speed conditioned inputs to the decoder.

Model	Heading Direction $R^2 \uparrow$	Average Speed $R^2 \uparrow$
C-VAE	0.636	0.617
SC-VAE-GR	0.756	0.634
SC-VAE-ND	0.959	0.627
SC-VAE-MALS	0.910	0.704
SC-VAE-MAQS	0.884	0.590
SC-VAE-MI	0.878	0.708

4.3 CONSISTENT MOTION SYNTHESIS

To evaluate whether our scrubbers maintained valid representations when reducing heading or speed decodability, we conditioned SC-VAE latents on random speeds and heading directions and calculated the resulting average speed and heading of the generated sequences (Table 1). We found that all scrubbers improved the consistency of conditionally generated sequences, with SC-VAE-ND and SC-VAE-MI being the best for heading and speed respectively. These results also suggest new strategies for improving conditional motion synthesis via enhanced subspace restrictiveness.

4.4 CLUSTERING DISENTANGLED REPRESENTATIONS

When clustering with Gaussian mixture models (GMMs), we found that the anisotropies due to nuisance variability in vanilla VAE and C-VAE representations determined the makeup of behavioral clusters, as they were comprised largely of behaviors with similar speeds or heading directions (Fig. 3a, e) as opposed to typical behaviorally relevant clusters (Fig. 7). Thus, these nuisance variables drive a trivial segmentation of behavioral space that obscures biologically meaningful behavioral identification. Scrubbing the C-VAE representations progressively reduced the influence of nuisance variables, increasing the variance of heading direction and speed within GMM clusters (Fig. 3b, f *top*). In the heading direction test case, SC-VAE-MI completely eliminated nuisance clustering and produced fully heading-mixed behavioral clusters. (Fig. 3d).

However, we found that MI scrubbing for speed was too strong and produced clusters no longer associated with typical coarse behavioral labels (e.g., walking, rearing, grooming). To further investigate, we trained a second vanilla VAE and labeled six walking clusters with differing distributions of speed (Fig. 3e). When comparing the latents in other models associated with these labeled walking clusters, the distributions of walking behaviors in the SC-VAE-MALS and SC-VAE-GR representations were better captured by a single cluster than other models (Fig. 3f *bottom*), demonstrating how scrubbing can combine behaviors previously distinguished only by nuisance variation (see B.6 for

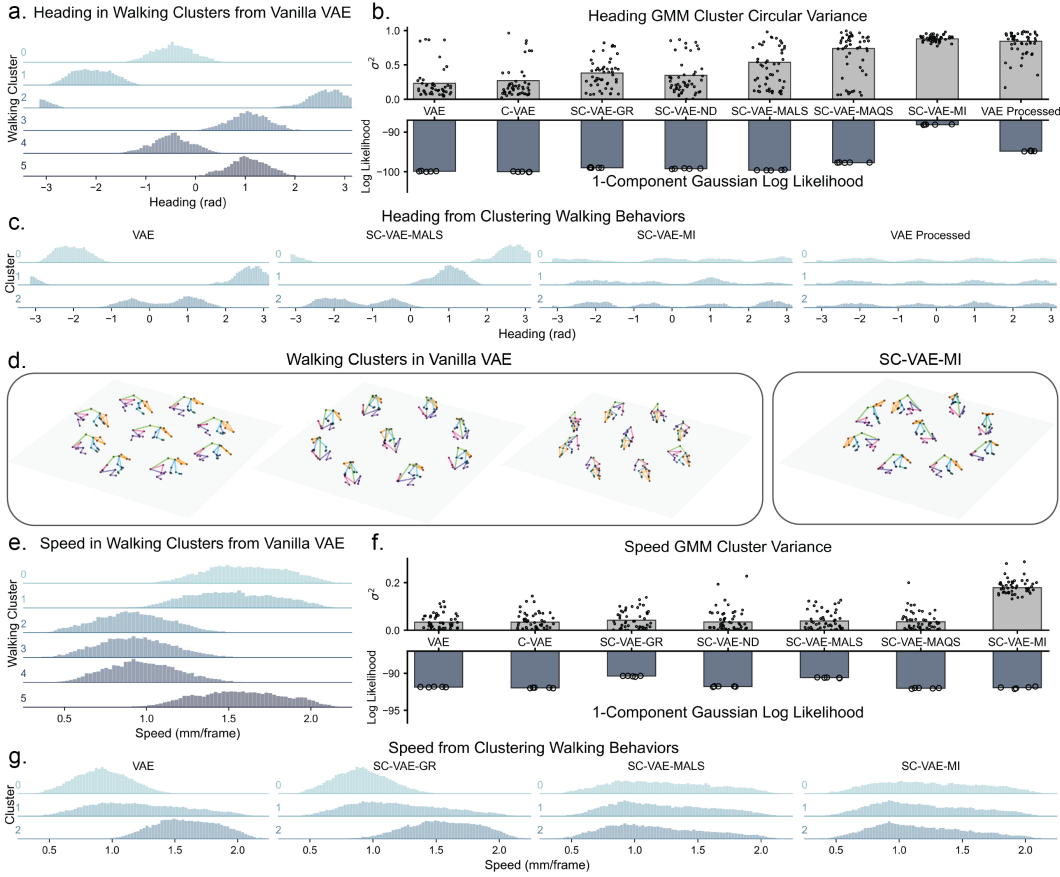


Figure 3: **Examining the effects of scrubbing on clustering.** (a) Heading direction distribution in walking GMM ($k = 50$) clusters identified from a separate VAE trained on not rotationally preprocessed data. (b) (*top*) Weighted average circular variance of heading by cluster. (*bottom*) 5-fold cross log-likelihood of a diagonal Gaussian component on the normalized latents of each model corresponding to the clusters in (a). (c) Histograms of heading in GMM clusters of VAE, SC-VAE-MALS, -MI, and VAE Processed latents corresponding to the clusters in (a). (d) Example walking clusters in VAE (*left*) and SC-VAE-MI (*right*) after scrubbing heading. (e) Speed distribution in walking GMM ($k = 50$) clusters identified from a separate VAE. (f) (*top*) Weighted average variance of speed by cluster. (*bottom*) 5-fold cross log-likelihood of a diagonal Gaussian component on the normalized latents per model corresponding to the clusters in (e). (g) Histograms of average speed in GMM ($k = 3$) clusters of VAE, SC-VAE-GR, -MALS, and -MI latents corresponding to the clusters in (e).

details on this metric). Further clustering of these walking behaviors in SC-VAE-MALS revealed completely speed-mixed clusters whereas the separation was still clearly present in vanilla VAE. Repeating this with heading scrubbing (separately identifying six walking clusters with different heading distributions), SC-VAE-MI was found to have the most ideal walking representation (Fig. 3c, d). These results suggest the need for disentanglement methods with weaker (-MALS) and stronger (-MI) assumptions for disentanglement which reflect the level of independence between nuisance variables and behavioral understanding.

4.5 NEUROLOGICAL DISEASE ANALYSIS

Subject-specific idiosyncrasies increase variability in behavioral expression across animals, potentially obscuring the effects of neurobehavioral perturbations. In our PD dataset, we found that scrubbing animal identity attenuated this variability, enhancing the detection of behavioral shifts in disease (PD) sessions. Using maximum mean discrepancy (MMD; B.6; Gretton et al., 2012; Goffinet et al.,

2021) to measure behavioral distribution similarity between recording sessions, we observed a large increase in similarity within conditions and decrease between conditions for the SC-VAE-QD model (Fig. 9). That is, a given disease session moved closer to the other disease sessions and farther from the healthy sessions, suggesting improved discriminability of disease-associated behavioral changes. We quantified this using an effect size metric, d , calculated as the MMD between a subject’s healthy and disease sessions relative to the MMD between healthy sessions across animals (Table 2 *left*, B.6). We also used a k-NN classifier to predict the type of session (healthy vs. disease) given a behavioral representation (Table 2 *middle*). SC-VAE-QD outperformed other models on these metrics. As a control, we also scrubbed the healthy vs. disease session label itself (‘Reverse Control’), which resulted in a significant decrease in both disease discriminability metrics.

Striatal immunostaining revealed another potential source of PD phenotype variability: not all animals experienced the same degree of dopaminergic denervation. More intact dopaminergic circuitry should be associated with fewer behavioral changes between healthy and PD sessions (Boix et al., 2015; Slézia et al., 2023). Thus, we expect behavioral representations better capturing these changes to be more correlated with the extent of denervation. While the healthy-disease MMD was correlated for all models, SC-VAE-QD strengthened the correlation (Table 2 *right*).

Table 2: **Scrubbing identity in a Parkinsonian mouse dataset.** Impact of identity scrubbing quantified as effect size (d) mean \pm SEM across animals, healthy vs. disease classification accuracy (%), and the correlation (Pearson r) of MMD behavioral change to dopamine denervation extent.

Model	Effect Size d \uparrow	Accuracy (%) \uparrow	Denervation correlation (r) \uparrow
VAE	1.30 ± 0.07	85.1	0.390
C-VAE	1.42 ± 0.08	87.0	0.401
SC-VAE-GR	1.58 ± 0.09	89.4	0.410
SC-VAE-QD	2.68 ± 0.19	91.9	0.474
Reverse Control	0.76 ± 0.04	66.6	0.289

5 CONCLUSION AND LIMITATIONS

This study presents a novel framework for disentangling nuisance behavioral or experimental variables by removing ("scrubbing") variable information from latent spaces via adversarial learning objectives. Our adaptive moving average, quadratic, and mutual information scrubbers are successful in producing behavioral representations that are linearly or nonlinearly invariant to nuisance variables, reducing behavioral over-segmentation and enhancing the interpretability of latent spaces. Existing approaches based on gradient reversal and adversarial networks generally only assume nonlinear scrubbing and, in our experience, are difficult to fine-tune. In contrast, our approach to training the adversarial scrubber based exponential moving averages of sufficient statistics is hyperparameter-free.

A limitation of our convolutional encoder-decoder architecture is that it represents fixed-length pose sequences as a single latent code, which constrains feature timescales and does not scale efficiently to long sequences. This issue could be addressed in future work by adopting a dynamic latent variable model. Additionally, our nuisance variable scope can be expanded to include factors on finer spatial and temporal scales, such as per frame or individual body part kinematics. Although all of the models presented in this paper were trained while scrubbing one nuisance variable at a time, SC-VAE can in principle be trained to jointly condition on multiple nuisance variables. This could increase the purity of behavioral representations, enable multifactor motion synthesis, and permit direct comparisons of nuisance variable effects within a common space. Future work should explore the effects of scrubbing multiple nuisance variables either jointly or individually.

Finally, we have focused on scrubbing out nuisance variables that are easily available (e.g., speed, heading direction, and animal identity), but it may not be obvious how to identify analogous variables or determine the correct level of disentanglement in more complex datasets (e.g., social). While believe our work is a step in the right direction, future work could focus on scrubbing in exploratory analyses, such as to fine-tune fully-unsupervised models. This work and future work seek to address the growing necessity for predictable and interpretable deep representation learning methods for neuroscientific research.

REFERENCES

- Martin Arjovsky and Léon Bottou. Towards principled methods for training generative adversarial networks. *arXiv preprint arXiv:1701.04862*, 2017.
- Mehdi Azabou, Michael Mendelson, Nauman Ahad, Maks Sorokin, Shantanu Thakoor, Carolina Urzay, and Eva Dyer. Relax, it doesn’t matter how you get there: A new self-supervised approach for multi-timescale behavior analysis. *Advances in Neural Information Processing Systems*, 36, 2024.
- Philip Bachman, R Devon Hjelm, and William Buchwalter. Learning representations by maximizing mutual information across views. *Advances in neural information processing systems*, 32, 2019.
- Praneet C Bala, Benjamin R Eisenreich, Seng Bum Michael Yoo, Benjamin Y Hayden, Hyun Soo Park, and Jan Zimmermann. Automated markerless pose estimation in freely moving macaques with openmonkeystudio. *Nature communications*, 11(1):4560, 2020.
- Mohamed Ishmael Belghazi, Aristide Baratin, Sai Rajeswar, Sherjil Ozair, Yoshua Bengio, Aaron Courville, and R Devon Hjelm. Mine: mutual information neural estimation. *arXiv preprint arXiv:1801.04062*, 2018.
- Gordon J Berman, Daniel M Choi, William Bialek, and Joshua W Shaevitz. Mapping the stereotyped behaviour of freely moving fruit flies. *Journal of The Royal Society Interface*, 11(99):20140672, 2014.
- Nicholas Bernstein. The coordination and regulation of movements. (*No Title*), 1967.
- William Bialek. On the dimensionality of behavior. *Proceedings of the National Academy of Sciences*, 119(18):e2021860119, May 2022. doi: 10.1073/pnas.2021860119. URL <https://www.pnas.org/doi/full/10.1073/pnas.2021860119>. Publisher: Proceedings of the National Academy of Sciences.
- Jordi Boix, Thomas Padel, and Gesine Paul. A partial lesion model of parkinson’s disease in mice—characterization of a 6-ohda-induced medial forebrain bundle lesion. *Behavioural brain research*, 284:196–206, 2015.
- Philemon Brakel and Yoshua Bengio. Learning independent features with adversarial nets for non-linear ica. *arXiv preprint arXiv:1710.05050*, 2017.
- Ricky TQ Chen, Xuechen Li, Roger B Grosse, and David K Duvenaud. Isolating sources of disentanglement in variational autoencoders. *Advances in neural information processing systems*, 31, 2018.
- Pengyu Cheng, Weituo Hao, Shuyang Dai, Jiachang Liu, Zhe Gan, and Lawrence Carin. Club: A contrastive log-ratio upper bound of mutual information. In *International conference on machine learning*, pp. 1779–1788. PMLR, 2020.
- Julia Costacurta, Lea Duncker, Blue Sheffer, Winthrop Gillis, Caleb Weinreb, Jeffrey Markowitz, Sandeep R Datta, Alex Williams, and Scott Linderman. Distinguishing discrete and continuous behavioral variability using warped autoregressive hmms. In S. Koyejo, S. Mohamed, A. Agarwal, D. Belgrave, K. Cho, and A. Oh (eds.), *Advances in Neural Information Processing Systems*, volume 35, pp. 23838–23850. Curran Associates, Inc., 2022.
- Sandeep Robert Datta, David J Anderson, Kristin Branson, Pietro Perona, and Andrew Leifer. Computational neuroethology: a call to action. *Neuron*, 104(1):11–24, 2019.
- Zheng Ding, Yifan Xu, Weijian Xu, Gaurav Parmar, Yang Yang, Max Welling, and Zhuowen Tu. Guided variational autoencoder for disentanglement learning. In *Proceedings of the IEEE/CVF conference on computer vision and pattern recognition*, pp. 7920–7929, 2020.
- Timothy W Dunn, Jesse D Marshall, Kyle S Severson, Diego E Aldarondo, David GC Hildebrand, Selmaan N Chettih, William L Wang, Amanda J Gellis, David E Carlson, Dmitriy Aronov, et al. Geometric deep learning enables 3d kinematic profiling across species and environments. *Nature methods*, 18(5):564–573, 2021.

- Babak Esmaeili, Hao Wu, Sarthak Jain, Alican Bozkurt, Narayanaswamy Siddharth, Brooks Paige, Dana H Brooks, Jennifer Dy, and Jan-Willem Meent. Structured disentangled representations. In *The 22nd International Conference on Artificial Intelligence and Statistics*, pp. 2525–2534. PMLR, 2019.
- Yaroslav Ganin and Victor Lempitsky. Unsupervised domain adaptation by backpropagation. In Francis Bach and David Blei (eds.), *Proceedings of the 32nd International Conference on Machine Learning*, volume 37 of *Proceedings of Machine Learning Research*, pp. 1180–1189, Lille, France, 07–09 Jul 2015a. PMLR. URL <https://proceedings.mlr.press/v37/ganin15.html>.
- Yaroslav Ganin and Victor Lempitsky. Unsupervised domain adaptation by backpropagation. In *International conference on machine learning*, pp. 1180–1189. PMLR, 2015b.
- Leilani H Gilpin, David Bau, Ben Z Yuan, Ayesha Bajwa, Michael Specter, and Lalana Kagal. Explaining explanations: An overview of interpretability of machine learning. In *2018 IEEE 5th International Conference on data science and advanced analytics (DSAA)*, pp. 80–89. IEEE, 2018.
- Jack Goffinet, Samuel Brudner, Richard Mooney, and John Pearson. Low-dimensional learned feature spaces quantify individual and group differences in vocal repertoires. *Elife*, 10:e67855, 2021.
- Ian Goodfellow, Jean Pouget-Abadie, Mehdi Mirza, Bing Xu, David Warde-Farley, Sherjil Ozair, Aaron Courville, and Yoshua Bengio. Generative adversarial networks. *Communications of the ACM*, 63(11):139–144, 2020.
- Arthur Gretton, Karsten M Borgwardt, Malte J Rasch, Bernhard Schölkopf, and Alexander Smola. A kernel two-sample test. *The Journal of Machine Learning Research*, 13(1):723–773, 2012.
- Chunzhi Gu, Jun Yu, and Chao Zhang. Learning disentangled representations for controllable human motion prediction. *Pattern Recognition*, 146:109998, 2024.
- Chuan Guo, Xinxin Zuo, Sen Wang, Shihao Zou, Qingyao Sun, Annan Deng, Minglun Gong, and Li Cheng. Action2motion: Conditioned generation of 3d human motions. In *Proceedings of the 28th ACM International Conference on Multimedia*, pp. 2021–2029, 2020.
- Chengan He, Jun Saito, James Zachary, Holly Rushmeier, and Yi Zhou. Nemf: Neural motion fields for kinematic animation. *Advances in Neural Information Processing Systems*, 35:4244–4256, 2022.
- Irina Higgins, Loic Matthey, Arka Pal, Christopher P Burgess, Xavier Glorot, Matthew M Botvinick, Shakir Mohamed, and Alexander Lerchner. beta-vae: Learning basic visual concepts with a constrained variational framework. *ICLR (Poster)*, 3, 2017.
- R Devon Hjelm, Alex Fedorov, Samuel Lavoie-Marchildon, Karan Grewal, Phil Bachman, Adam Trischler, and Yoshua Bengio. Learning deep representations by mutual information estimation and maximization. *arXiv preprint arXiv:1808.06670*, 2018.
- Zhiwu Huang, Chengde Wan, Thomas Probst, and Luc Van Gool. Deep learning on lie groups for skeleton-based action recognition. In *Proceedings of the IEEE conference on computer vision and pattern recognition*, pp. 6099–6108, 2017.
- Ilyes Khemakhem, Diederik Kingma, Ricardo Monti, and Aapo Hyvarinen. Variational autoencoders and nonlinear ica: A unifying framework. In *International Conference on Artificial Intelligence and Statistics*, pp. 2207–2217. PMLR, 2020.
- Hyunjik Kim and Andriy Mnih. Disentangling by factorising. In *International conference on machine learning*, pp. 2649–2658. PMLR, 2018.
- Diederik P Kingma and Max Welling. Auto-encoding variational bayes. *arXiv preprint arXiv:1312.6114*, 2013.
- Francesco Locatello, Stefan Bauer, Mario Lucic, Gunnar Raetsch, Sylvain Gelly, Bernhard Schölkopf, and Olivier Bachem. Challenging common assumptions in the unsupervised learning of disentangled representations. In *international conference on machine learning*, pp. 4114–4124. PMLR, 2019.

- Ilya Loshchilov and Frank Hutter. Decoupled weight decay regularization. *arXiv preprint arXiv:1711.05101*, 2017.
- Kevin Luxem, Petra Mocellin, Falko Fuhrmann, Johannes Kürsch, Stephanie R Miller, Jorge J Palop, Stefan Remy, and Pavol Bauer. Identifying behavioral structure from deep variational embeddings of animal motion. *Communications Biology*, 5(1):1267, 2022.
- Jesse D Marshall, Diego E Aldarondo, Timothy W Dunn, William L Wang, Gordon J Berman, and Bence P Ölveczky. Continuous whole-body 3d kinematic recordings across the rodent behavioral repertoire. *Neuron*, 109(3):420–437, 2021.
- Jesse D. Marshall, Tianqing Li, Joshua H. Wu, and Timothy W. Dunn. Leaving flatland: Advances in 3D behavioral measurement. *Current Opinion in Neurobiology*, 73:102522, April 2022. ISSN 1873-6882. doi: 10.1016/j.conb.2022.02.002.
- Michael H McCullough and Geoffrey J Goodhill. Unsupervised quantification of naturalistic animal behaviors for gaining insight into the brain. *Current Opinion in Neurobiology*, 70:89–100, 2021.
- Young-Il Moon, Balaji Rajagopalan, and Upmanu Lall. Estimation of mutual information using kernel density estimators. *Physical Review E*, 52(3):2318, 1995.
- Kevin P Murphy. *Machine learning: a probabilistic perspective*. MIT press, 2012.
- Simon Musall, Matthew T. Kaufman, Ashley L. Juavinett, Steven Gluf, and Anne K. Churchland. Single-trial neural dynamics are dominated by richly varied movements. *Nature Neuroscience*, 22(10):1677–1686, October 2019. ISSN 1546-1726. doi: 10.1038/s41593-019-0502-4. URL <https://www.nature.com/articles/s41593-019-0502-4>. Number: 10 Publisher: Nature Publishing Group.
- Tanmay Nath, Alexander Mathis, An Chi Chen, Amir Patel, Matthias Bethge, and Mackenzie Weygandt Mathis. Using DeepLabCut for 3D markerless pose estimation across species and behaviors. *Nature Protocols*, 14(7):2152–2176, July 2019. ISSN 1750-2799. doi: 10.1038/s41596-019-0176-0.
- Eric J Nestler and Steven E Hyman. Animal models of neuropsychiatric disorders. *Nature neuroscience*, 13(10):1161–1169, 2010.
- Ali Nourizonoz, Robert Zimmermann, Chun Lum Andy Ho, Sebastien Pellat, Yannick Ormen, Clément Prévost-Solié, Gilles Reymond, Fabien Pifferi, Fabienne Aujard, Anthony Herrel, and Daniel Huber. EthoLoop: automated closed-loop neuroethology in naturalistic environments. *Nature Methods*, 17(10):1052–1059, October 2020. ISSN 1548-7105. doi: 10.1038/s41592-020-0961-2. URL <https://doi.org/10.1038/s41592-020-0961-2>.
- Talmo D Pereira, Nathaniel Tabris, Arie Matsliah, David M Turner, Junyu Li, Shruthi Ravindranath, Eleni S Papadoyannis, Edna Normand, David S Deutsch, Z Yan Wang, et al. Sleap: A deep learning system for multi-animal pose tracking. *Nature methods*, 19(4):486–495, 2022.
- Mathis Petrovich, Michael J. Black, and Gül Varol. Action-conditioned 3d human motion synthesis with transformer vae. In *Proceedings of the IEEE/CVF International Conference on Computer Vision (ICCV)*, pp. 10985–10995, October 2021a.
- Mathis Petrovich, Michael J Black, and Gül Varol. Action-conditioned 3d human motion synthesis with transformer vae. In *Proceedings of the IEEE/CVF International Conference on Computer Vision*, pp. 10985–10995, 2021b.
- Ben Poole, Sherjil Ozair, Aaron Van Den Oord, Alex Alemi, and George Tucker. On variational bounds of mutual information. In *International Conference on Machine Learning*, pp. 5171–5180. PMLR, 2019.
- Alec Radford. Unsupervised representation learning with deep convolutional generative adversarial networks. *arXiv preprint arXiv:1511.06434*, 2015.

- Eduardo Hugo Sanchez, Mathieu Serrurier, and Mathias Ortner. Learning disentangled representations via mutual information estimation. In *Computer Vision—ECCV 2020: 16th European Conference, Glasgow, UK, August 23–28, 2020, Proceedings, Part XXII 16*, pp. 205–221. Springer, 2020.
- Giovanna Scaramuzzino, Federico Becattini, and Alberto Del Bimbo. Attribute disentanglement with gradient reversal for interactive fashion retrieval. *Pattern Recognition Letters*, 172:203–212, 2023.
- Jiayi Shen, Xiaohan Chen, Howard Heaton, Tianlong Chen, Jialin Liu, Wotao Yin, and Zhangyang Wang. Learning a minimax optimizer: A pilot study. In *International Conference on Learning Representations*, 2020.
- Changhao Shi, Sivan Schwartz, Shahar Levy, Shay Achvat, Maisan Abboud, Amir Ghanayim, Jackie Schiller, and Gal Mishne. Learning disentangled behavior embeddings. *Advances in neural information processing systems*, 34:22562–22573, 2021.
- Rui Shu, Yining Chen, Abhishek Kumar, Stefano Ermon, and Ben Poole. Weakly supervised disentanglement with guarantees. *arXiv preprint arXiv:1910.09772*, 2019.
- Andrea Slézia, Panna Hegedüs, Evgeniia Rusina, Katalin Lengyel, Nicola Solari, Attila Kaszas, Diána Balázsfi, Boris Botzanowski, Emma Acerbo, Florian Missey, et al. Behavioral, neural and ultrastructural alterations in a graded-dose 6-ohda mouse model of early-stage parkinson’s disease. *Scientific Reports*, 13(1):19478, 2023.
- Kihyuk Sohn, Honglak Lee, and Xinchun Yan. Learning structured output representation using deep conditional generative models. *Advances in neural information processing systems*, 28, 2015.
- Elsbeth A. Van Dam, Lucas P. J. J. Noldus, and Marcel A. J. Van Gerven. Disentangling rodent behaviors to improve automated behavior recognition. *Frontiers in Neuroscience*, 17, July 2023. ISSN 1662-453X. doi: 10.3389/fnins.2023.1198209. URL <https://www.frontiersin.org/journals/neuroscience/articles/10.3389/fnins.2023.1198209/full>. Publisher: Frontiers.
- Raviteja Vemulapalli, Felipe Arrate, and Rama Chellappa. Human action recognition by representing 3d skeletons as points in a lie group. In *Proceedings of the IEEE conference on computer vision and pattern recognition*, pp. 588–595, 2014.
- Lukas von Ziegler, Oliver Sturman, and Johannes Bohacek. Big behavior: challenges and opportunities in a new era of deep behavior profiling. *Neuropsychopharmacology*, 46(1):33–44, 2021.
- Caleb Weinreb, Jonah Pearl, Sherry Lin, Mohammed Abdal Monium Osman, Libby Zhang, Sidharth Annapragada, Eli Conlin, Red Hoffman, Sofia Makowska, Winthrop F Gillis, et al. Keypoint-moseq: parsing behavior by linking point tracking to pose dynamics. *BioRxiv*, 2023.
- Matthew R Whiteway, Dan Biderman, Yoni Friedman, Mario Dipoppa, E Kelly Buchanan, Anqi Wu, John Zhou, Niccolò Bonacchi, Nathaniel J Miska, Jean-Paul Noel, et al. Partitioning variability in animal behavioral videos using semi-supervised variational autoencoders. *PLoS computational biology*, 17(9):e1009439, 2021.
- Alexander B. Wiltschko, Matthew J. Johnson, Giuliano Iurilli, Ralph E. Peterson, Jesse M. Katon, Stan L. Pashkovski, Victoria E. Abraira, Ryan P. Adams, and Sandeep Robert Datta. Mapping sub-second structure in mouse behavior. *Neuron*, 88(6):1121–1135, 2015a. ISSN 0896-6273. doi: <https://doi.org/10.1016/j.neuron.2015.11.031>. URL <https://www.sciencedirect.com/science/article/pii/S0896627315010375>.
- Alexander B. Wiltschko, Matthew J. Johnson, Giuliano Iurilli, Ralph E. Peterson, Jesse M. Katon, Stan L. Pashkovski, Victoria E. Abraira, Ryan P. Adams, and Sandeep Robert Datta. Mapping Sub-Second Structure in Mouse Behavior. *Neuron*, 88(6):1121–1135, December 2015b. ISSN 0896-6273. doi: 10.1016/j.neuron.2015.11.031. URL <https://www.ncbi.nlm.nih.gov/pmc/articles/PMC4708087/>.

- Alexander B. Wiltchko, Tatsuya Tsukahara, Ayman Zeine, Rockwell Anyoha, Winthrop F. Gillis, Jeffrey E. Markowitz, Ralph E. Peterson, Jesse Katon, Matthew J. Johnson, and Sandeep Robert Datta. Revealing the structure of pharmacobehavioral space through motion sequencing. *Nature Neuroscience*, 23(11):1433–1443, November 2020. ISSN 1546-1726. doi: 10.1038/s41593-020-00706-3.
- Anqi Wu, Estefany Kelly Buchanan, Matthew Whiteway, Michael Schartner, Guido Meijer, Jean-Paul Noel, Erica Rodriguez, Claire Everett, Amy Norovich, Evan Schaffer, et al. Deep graph pose: a semi-supervised deep graphical model for improved animal pose tracking. *Advances in Neural Information Processing Systems*, 33:6040–6052, 2020.
- Yilun Xu, Shengjia Zhao, Jiaming Song, Russell Stewart, and Stefano Ermon. A theory of usable information under computational constraints. In *International Conference on Learning Representations*, 2020a. URL <https://openreview.net/forum?id=r1eBeyHFDH>.
- Yilun Xu, Shengjia Zhao, Jiaming Song, Russell Stewart, and Stefano Ermon. A theory of usable information under computational constraints. *arXiv preprint arXiv:2002.10689*, 2020b.
- Daiyao Yi and Shreya Saxena. Modeling the behavior of multiple subjects using a cauchy-schwarz regularized partitioned subspace variational autoencoder (cs-ps-vae). In *2022 44th Annual International Conference of the IEEE Engineering in Medicine & Biology Society (EMBC)*, pp. 497–503. IEEE, 2022.
- Long Zhao, Yuxiao Wang, Jiaping Zhao, Liangzhe Yuan, Jennifer J Sun, Florian Schroff, Hartwig Adam, Xi Peng, Dimitris Metaxas, and Ting Liu. Learning view-disentangled human pose representation by contrastive cross-view mutual information maximization. In *Proceedings of the IEEE/CVF Conference on Computer Vision and Pattern Recognition*, pp. 12793–12802, 2021.
- Yi Zhou, Connelly Barnes, Jingwan Lu, Jimei Yang, and Hao Li. On the continuity of rotation representations in neural networks. In *Proceedings of the IEEE/CVF conference on computer vision and pattern recognition*, pp. 5745–5753, 2019.
- Christian Zimmermann, Artur Schneider, Mansour Alyahyay, Thomas Brox, and Ilka Diester. Freipose: a deep learning framework for precise animal motion capture in 3d spaces. *BioRxiv*, pp. 2020–02, 2020.

A METHOD DETAILS

A.1 POSE PREPROCESSING

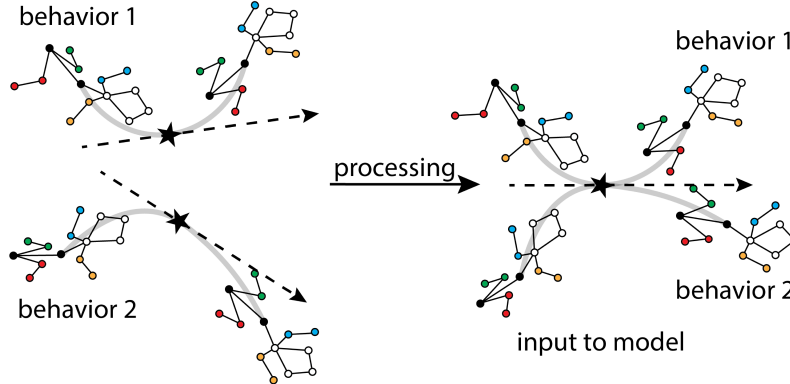


Figure 4: **Aligning pose trajectories.** All pose sequences are translated and aligned so that the central frame is globally centered and rotated to face in a standard direction. This representation preserves important trajectory information. We decompose our pose sequences into local joint rotations and global root position as is commonly done in 3D deep pose methods (e.g., Petrovich et al., 2021b; He et al., 2022).

A.2 SCRUBBERS

Scrubbing by adaptive moving average least square (SC-VAE-MALS)

Consider a linear decoder:

$$f_{\psi}(\mathbf{z}) = \psi \mathbf{z} = \hat{\mathbf{v}} \quad (7)$$

where $\psi = \psi^0(\psi^1 + \beta \mathbf{I})^{-1}$, which can be evaluated using the loss:

$$L(\mathbf{z}, \mathbf{v}; \psi) = \|\mathbf{v} - f_{\psi}(\mathbf{z})\|_2^2 \quad (8)$$

Algorithm 1 SC-VAE-MALS

Initialize network parameters

ϕ, θ

Initialize linear estimator parameters

$\hat{\psi} \in \mathbb{R}^{N \times D}$

Initialize forgetting factor

$\alpha \in (0, 1)$

Initialize L2-regularization coefficient

$\beta \in \mathbb{R}$

repeat

 Draw batch with K samples

$(\mathbf{x}_k, \mathbf{v}_k \in \mathbb{R}^{N \times K}), \mathbf{z}_k \sim q_{\phi}(\cdot | \mathbf{x}_k) \in \mathbb{R}^{D \times K}$

 Calculate decoder loss:

$L_{\text{Scrub}} = L(\mathbf{z}_k, \mathbf{v}_k; \psi)$

 Update ψ based on the normal equations for ordinary least squares regression:

$\hat{\psi}_{k+1}^0 = (1 - \alpha) \mathbf{v}_k \mathbf{z}_k^{\top} + \alpha \hat{\psi}_k^0$

$\hat{\psi}_{k+1}^1 = (1 - \alpha) \mathbf{z}_k \mathbf{z}_k^{\top} + \alpha \hat{\psi}_k^1$

 Update network parameters:

$\phi \leftarrow \phi + \nabla [L_{\text{Scrub}} + L_{\text{ELBO}} + L_{\text{Recon}}]$

$\theta \leftarrow \theta + \nabla [L_{\text{Recon}}]$

until convergence

Scrubbing by adaptive quadratic discriminators (SC-VAE-QD)

Consider the class-conditional Bayes classifier:

$$f_\psi(\mathbf{z}) = p(v = c | \mathbf{z}) \quad (9)$$

with likelihood,

$$p(z | v = c) = N(\mathbf{z} | \mu^c, \Sigma^c). \quad (10)$$

For multi-class problems, we maintain a *one vs rest* estimator per class, $\psi = \{\mu^c, \Sigma^c, \mu^{c'}, \Sigma^{c'} \mid \forall c \in C\}$. This estimator can be evaluated based on the Gaussian log-likelihood:

$$L(\mathbf{z}, v; \psi^c) = \ell(\mu^c, \Sigma^c | \mathbf{z}, v = c) + \ell(\mu^{c'}, \Sigma^{c'} | \mathbf{z}, v \neq c). \quad (11)$$

Algorithm 2 SC-VAE-QD

```

Initialize network parameters
 $\phi, \theta$ 
Initialize parameters of two classifiers
 $\psi_a, \psi_b$ 
 $\lambda \leftarrow \alpha \mathbf{1}_C, \alpha \in (0, 1)$ 
repeat
  Draw minibatch of  $(\mathbf{x}_k, \mathbf{v}_k, \mathbf{z}_k)$  as in Alg 1
   $L_{\text{scrub}} = 0$ 
  for  $c \in C$  do
    Evaluate the Gaussian log-likelihood ratio for each classifier and average scrubbing loss:
     $L_{\text{scrub}} = L_{\text{scrub}} + \frac{1}{K} \sum_K L(\mathbf{z}_k, v_k; \psi^c)$ 
    Update class means and covariances for both estimators:
     $\mu^c = (1 - \alpha^c) \mathbb{E}_{\mathbf{v}_k=c}[\mathbf{z}_k] + \alpha^c \mu^c$ 
     $\Sigma^c = \text{Cov}_{\mathbf{v}_k=c}[\mathbf{z}_k, \mathbf{z}_k]$ 
     $\mu^{c'} = (1 - \alpha^{c'}) \mathbb{E}_{\mathbf{v}_k \neq c}[\mathbf{z}_k] + \alpha^{c'} \mu^{c'}$ 
     $\Sigma^{c'} = \text{Cov}_{\mathbf{v}_k \neq c}[\mathbf{z}_k, \mathbf{z}_k]$ 
  end for
  Update network parameters as in Alg 1
until convergence

```

Automatically tuning forgetting factor

One of the core features of the moving average scrubbing methods (SC-VAE-MALS and -QD) is the automatic tuning of the forgetting factor, λ . Given a discriminator function, $f_\psi(\mathbf{z})$, and a minimization objective, $L(z, v; \psi)$, we simultaneously estimate two discriminators from the same function family, $f_{\psi_a}(\mathbf{z})$ and $f_{\psi_b}(\mathbf{z})$. The estimators use distinct forgetting factors, α_a and α_b , with a fixed offset ϵ . We tune both α_a and α_b in the direction of the better performing discriminator.

Algorithm 3 Automatically tuning forgetting factor (λ)

```

 $\psi_a, \psi_b \leftarrow$  Initialize parameters of two discriminators
Initialize forgetting factors with fixed offset:  $\epsilon$ 
 $\alpha_a \in (0, 1 - \epsilon)$ 
 $\alpha_b \leftarrow \alpha_a + \epsilon$ 
repeat
  Draw minibatch with  $K$  samples:
   $(\mathbf{x}_k, \mathbf{v}_k), \mathbf{z}_k \sim q_\phi(\cdot | \mathbf{x}_k) \in \mathbb{R}^{D \times K}$ 
  Average the losses of the two discriminators to obtain the scrubbing loss
   $L_{\text{scrub}} = \frac{1}{2} [L(\mathbf{z}_k, \mathbf{v}_k; \psi_a) + L(\mathbf{z}_k, \mathbf{v}_k; \psi_b)]$ 
  Forgetting factors step by  $\Delta$  in the direction of the better decoder between  $f_{\psi_a}$  and  $f_{\psi_b}$ 
  if  $L(\mathbf{z}_k, \mathbf{v}_k; \psi_a) > L(\mathbf{z}_k, \mathbf{v}_k; \psi_b)$  then
     $\alpha_a = \max(\alpha_a - \Delta, 0)$ 
     $\alpha_b = \alpha_a + \epsilon$ 
  else
     $\alpha_b = \min(\alpha_b + \Delta, 1)$ 
     $\alpha_a = \alpha_b - \epsilon$ 
  end if
  Continue with updating  $\psi_a, \psi_b, \phi$ , and  $\theta$  as described in Algorithms 1 and 2.
until convergence

```

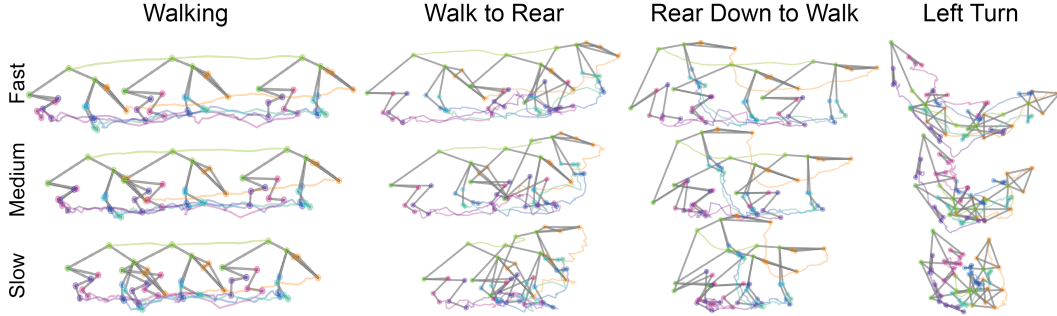
B EXPERIMENT DETAILS**B.1 CONDITIONAL MOTION GENERATION**

Figure 5: **Enabling conditional motion generation.** By manually adjusting the value of the conditioned variable, \mathbf{v}_t , we enable granular control over this variable in the generated output without changing the gross behavioral category. Here we change the conditioned speed and are able to adjust the speed of a behavior.

B.2 LATENT VISUALIZATIONS

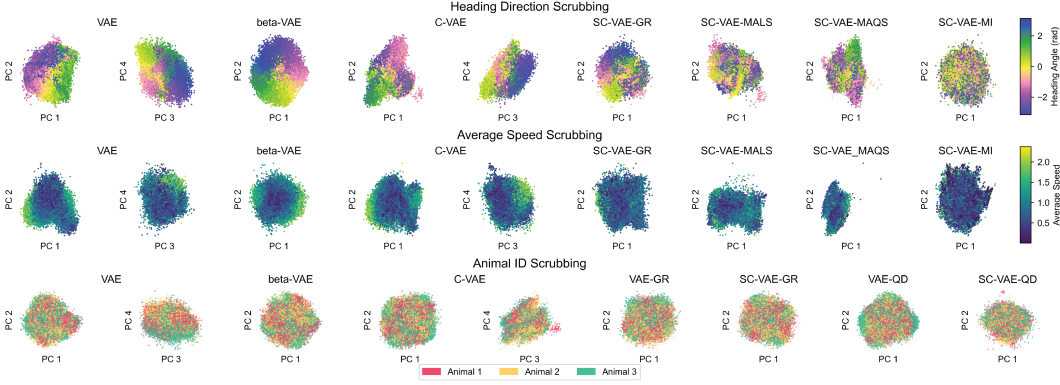


Figure 6: **PCA visualizations.** Projections of vanilla and scrubbed model representations to the top principal component dimensions, colored by heading (*top*), speed (*mid*), and identity (*bottom*).

B.3 OBTAINING BEHAVIORAL MOTIFS

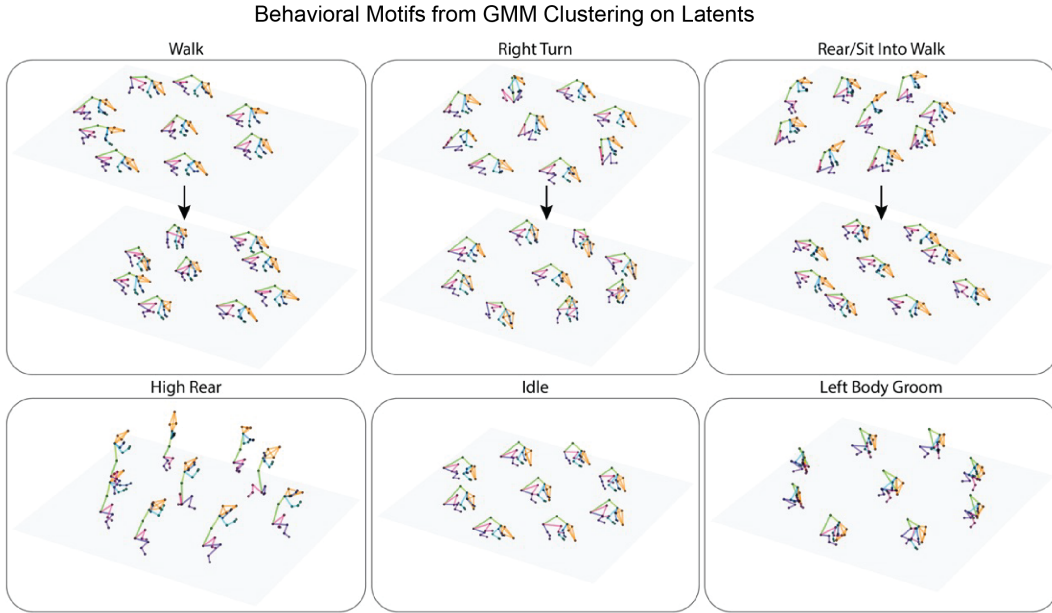


Figure 7: **Example motifs from GMM clustering.** Motifs extracted from our models' deep representations qualitatively reveal interpretable behavioral motifs.

B.4 NUISANCE VARIABLE DETAILS

Average speed Average speed is a 3-dimensional vector corresponding to: (1) the total displacement of the root keypoint during a window (51 frames here), (2) the average speed of the spine and head relative to the root keypoint, and (3) the average speed of the limbs relative to the attached spine keypoint.

Heading direction Given a pose sequence, we calculate the yaw, α , of the *mid-spine* \rightarrow *front-spine* segment for the central frame of a pose sequence (i.e., the 26th frame of a 51 frame sequence in this paper). The final heading direction used by the scrubber is $[\sin \alpha, \cos \alpha]^\top$.

Animal identity We represent all categorical nuisance variables with one-hot encoding vectors.

B.5 SCRUBBING IDENTITY IN VAE WITHOUT CONDITIONING

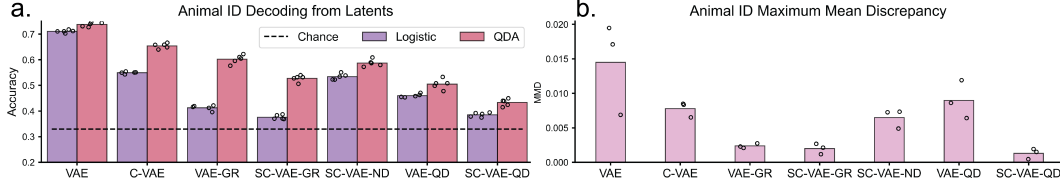


Figure 8: **Decoding identity from scrubbed latents.** (a) Classification accuracy for animal identity using logistic regression and quadratic discriminates. (b) Paired inter-individual MMD.

Given the need to maintain a reasonable reconstruction error when learning a scrubbed variational distribution, it follows that conditioning would be required when disentangling variables such as speed or heading. However, conditioning does not seem to be as intuitively necessary when disentangling variables, such as animal identity, which do not directly contribute to the reconstruction error. Despite this, we find that conditioning with one-hot encodings on animal identity improves the scrubbing performance, as the linear and quadratic decodability of identity is reduced compared to scrubbing identity in a standard VAE (VAE-GR and VAE-QD in Fig. 8a). SC-VAE representations also reduced the paired maximum mean discrepancy (MMD) (Gretton et al., 2012) between individuals (Fig. 8b).

B.6 METRIC DEFINITIONS

One-component Gaussian log-likelihood Given a mean-centered and standardized latent representation over a dataset, we split the walking behaviors \mathbf{Z}^{walk} into $\mathbf{Z}_{train}^{walk}$ and \mathbf{Z}_{test}^{walk} . We use the mean μ and diagonal covariance $\sigma^2 \mathbf{I}$ of $\mathbf{Z}_{train}^{walk}$ to calculate the Gaussian log-likelihood of \mathbf{Z}_{test}^{walk} .

$$\ln p(\mathbf{z} \mid \mu, \sigma^2 \mathbf{I}) = -\frac{1}{2} [d \ln 2\pi + \ln |\sigma^2 \mathbf{I}| + (\mathbf{z} - \mu)^\top (\sigma^2 \mathbf{I})^{-1} (\mathbf{z} - \mu)] \quad (12)$$

Thus, we quantify the level at which walking clusters of different speeds or heading directions can be represented by a single, merged Gaussian distribution. We cross-validated this over five folds.

Maximum mean discrepancy We use maximum mean discrepancy (MMD) (Gretton et al., 2012) to define a distance between two latent behavioral distributions with M and N samples, $\mathbf{X} \in \mathbb{R}^{M \times D}$ and $\mathbf{Y} \in \mathbb{R}^{N \times D}$. Given a radial basis kernel function with bandwidth h ,

$$k(\mathbf{z}, \mathbf{z}') = \exp\left(-\frac{\|\mathbf{z} - \mathbf{z}'\|^2}{h}\right), \quad (13)$$

MMD is defined as,

$$\begin{aligned} D_{MMD}(\mathbf{X}, \mathbf{Y}) = & \frac{1}{M(M-1)} \sum_{i=1}^M \sum_{j \neq i}^M k(\mathbf{x}_i, \mathbf{x}_j) + \frac{1}{N(N-1)} \sum_{i=1}^N \sum_{j \neq i}^N k(\mathbf{y}_i, \mathbf{y}_j) \\ & + \frac{2}{MN} \sum_{i=1}^M \sum_{j=1}^N k(\mathbf{x}_i, \mathbf{y}_j). \end{aligned} \quad (14)$$

Using the heuristic in Gretton et al. (2012), we define h to be the median Euclidean distance in the aggregate sample $[\mathbf{X}, \mathbf{Y}]$. When visualizing the paired MMD between all available sessions (72 total) in Fig. 9, we qualitatively find increased differences across conditions compared to within conditions. We describe our quantification of this effect below.

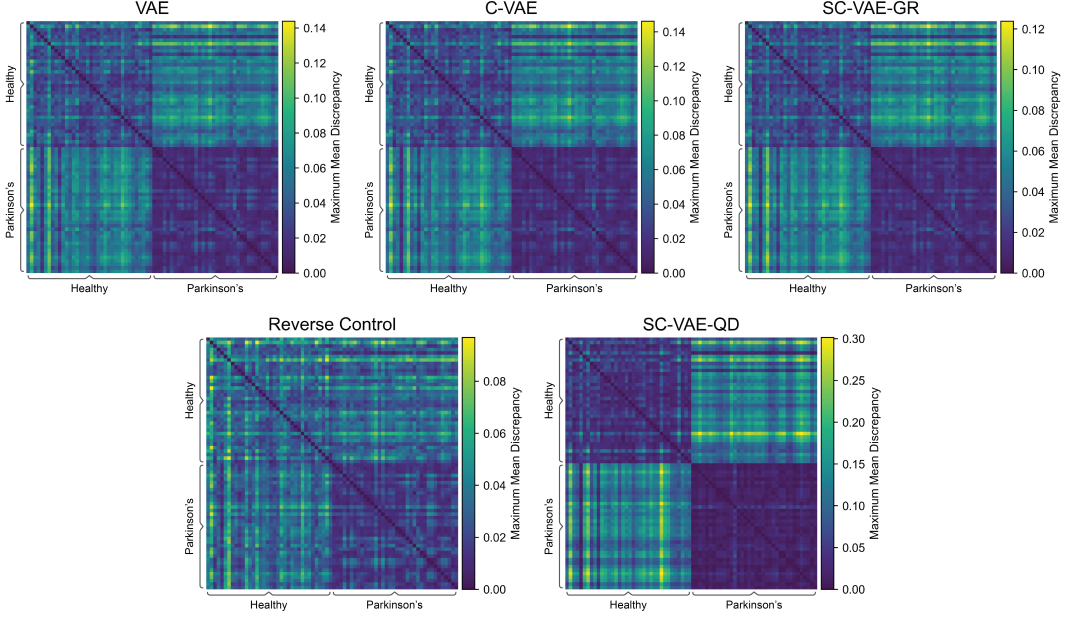


Figure 9: **Pairwise maximum mean discrepancy.** For each session (healthy or diseased) of each animal, we calculated the maximum mean discrepancy between their behavioral distribution. Qualitatively, the difference in the cross-condition MMD (*top-right* and *bottom-left* quadrants) vs the in-condition MMD (*top-left* and *bottom-right* quadrants) is more pronounced in SC-VAE-QD compared to other models. This demonstrates the enhanced disease discriminability in our scrubbed models.

In Sec. 4.5, we compare the healthy-disease discrepancy to the inter-individual discrepancy. Given a dataset of I individuals where \mathbf{H}_i is the healthy behavioral distribution and \mathbf{D}_i is the diseased behavioral distribution of animal i , we calculate two metrics akin to statistical effect size.

$$[d_H]_i = \frac{(I-1) * D_{MMD}(\mathbf{H}_i, \mathbf{D}_i)}{\sum_{j \neq i} D_{MMD}(\mathbf{H}_i, \mathbf{H}_j)} \quad (15)$$

$$[d_D]_i = \frac{(I-1) * D_{MMD}(\mathbf{H}_i, \mathbf{D}_i)}{\sum_{j \neq i} D_{MMD}(\mathbf{D}_i, \mathbf{D}_j)} \quad (16)$$

Cohen’s effect size is more similar to the cross-condition distance normalized to the variance within the control condition (healthy), thus we report d_H in Table 2. Both metrics are reported in Table 3. Finally, we construct a k-nearest neighbor classifier ($k = 35$) to classify behavioral distributions using our MMD distance to quantify the changes in decoding accuracy of the disease label due to scrubbing.

Table 3: **Maximum mean discrepancy metrics.** We quantify the difference in an animal’s cross-condition representations compared to the average in-condition difference.

Model	Effect Size	
	$d_H \uparrow$	$d_D \uparrow$
VAE	1.30 ± 0.07	2.82 ± 0.21
C-VAE	1.42 ± 0.08	3.20 ± 0.24
SC-VAE-GR	1.58 ± 0.09	3.44 ± 0.25
SC-VAE-QD	2.68 ± 0.19	7.02 ± 0.63
Reverse Control	0.76 ± 0.04	1.53 ± 0.12

C MODEL TRAINING DETAILS

C.1 MODEL ARCHITECTURES

Table 4: **Residual block architecture.**

Layer	Kernel	Stride	Padding	Activation	Normalization	Channels out
Input	-	-	-	None	None	in_channel
Conv1D 1	3	2	1	PReLU	Batch	out_channel//2
Conv1D 2	3	1	1	None	None	out_channel
Conv1D skip	3	2	1	None	None	out_channel
Add	-	-	-	PReLU	Batch	out_channel

Table 5: **Residual block transpose architecture.**

Layer	Kernel	Stride	Padding	Activation	Normalization	Channels out
Input	-	-	-	None	None	in_channel
Conv1D ^T 1	3	1	1	PReLU	Batch	in_channel//2
Conv1D ^T 2	3	2	1	None	None	out_channel
Upsample by 2	-	-	-	None	None	out_channel
Conv1D skip	4	1	1	None	None	out_channel
Add	-	-	-	PReLU	Batch	out_channel

Table 6: **Representation encoder architecture.**

Layer	Kernel	Stride	Padding	Activation	Normalization	Output
Input	-	-	-	None	None	51×111
Conv1D	7	1	3	PReLU	None	51×128
Residual 1	3	2	1	PReLU	Batch	26×256
Residual 2	3	2	1	PReLU	Batch	13×512
Flatten	-	-	-	None	None	6656
Dense (μ)	-	-	-	PReLU	None	64
Dense (σ)	-	-	-	PReLU	None	64

Table 7: **Representation decoder architecture.** c is the dimension of the disentanglement variable

Layer	Kernel	Stride	Padding	Activation	Normalization	Output
Encoded input	-	-	-	None	None	$64 + c$
Dense	-	-	-	PReLU	None	6656
Unflatten	-	-	-	None	None	13×512
Residual ^T 1	3	2	1	PReLU	Batch	25×256
Residual ^T 2	3	2	1	PReLU	Batch	49×128
Conv1D ^T	9	1	3	Tanh	None	51×111

Table 8: **Gradient reversal scrubber.** Uses ReLU activation for all dense layers. c is the dimension of the disentanglement variable

Layer	Input	Output
Gradient reversal (before MLP Ensemble)	-	-
MLP 1		
Dense 1	64	64
Dense 2	64	64
Dense 3	64	c
MLP 2		
Dense 1	64	64
Dense 2	64	c
MLP 3		
Dense 1	64	64
Dense 2	64	32
Dense 3	32	c
MLP 4		
Dense 1	64	128
Dense 2	128	128
Dense 3	128	c

C.2 TRAINING DETAILS AND HYPERPARAMETERS

We standardized training across models comparisons such that the following are true for all models.

- Models were trained on NVIDIA A100 and V100 GPUs.
- Models were trained using AdamW optimizer (Loshchilov & Hutter, 2017) with a learning rate of 0.0001 and gradient clipping at 10,000.
- Losses for models had the same weights for joint position error and the VAE ELBO loss.
- Models were trained for 400 iterations over the training dataset with batch sizes of 2048.
- The model architecture described in Section C.1 was not changed across tasks.
- We used a pose sequence window size of 51 frames.
- The size of the latent dimension \mathbf{z}_t was 64 for the results in Sections 4.4-4.2 and 32 for the results in Section 4.5.

To ensure fair comparison across models, we limited hyperparameter-tuning to only method-relevant hyperparameters. General hyperparameters and optimizers were chosen to improve the joint position error in vanilla VAE reconstructions. These hyperparameters as described above were held constant across all SC-VAE models.

Parameter tuning for SC-VAE scrubbers largely revolved around tuning the λ of the $L_{\text{scrub}}(\phi)$ loss. In most cases, increasing lambda increased strength of the scrubber up to its linear or nonlinear assumptions. However, when λ was too large, we found some cases of posterior collapse or mode collapse, primarily in the neural network scrubbing models (SC-VAE-GR and -ND). For SC-VAE-GR, we were additionally required to tune the scaling factor of the gradient reversal layer α . For SC-VAE-ND, we found performance changes due to the number of discriminator training iterations in between

C-VAE iterations. If too few iterations were taken, the discriminator would underfit and vice versa. Due to our increment strategy for forgetting factors (Algorithm A.2), in training SC-VAE-MALS and SC-VAE-QD, λ was the only required parameter to tune. In the polynomial extensions to the moving average algorithm (SC-VAE-MAQS), we found better performance with non-zero L2 regularization, β . Finally, for SC-VAE-MI, we additionally tuned the h parameter determining the spherical width of the kernel.

Models were selected based on the level of invariance in their representations to the scrubbed nuisance variable (i.e., the metrics in Fig. 2). The results in Sections 4.4-4.2 were all calculated on the same set of models. Models were re-trained from scratch on the Parkinsonian dataset to obtain the results in Section 4.5.

Table 9: Hyperparameter search. We list the hyperparameters and values over which we trained models for our experiments. We applied grid search for methods with more than one hyperparameter.

Model	Hyperparameters	Values
SC-VAE-GR	λ	10, 20, 50, 100
	α	0.8, 1.0, 1.2
SC-VAE-ND	λ	10, 50, 100
	n_{iter}	1, 10, 50, 100
SC-VAE-MALS	λ	10, 20, 50
SC-VAE-MAQS	λ	5, 10, 20
	β	0.25, 0.5, 0.75
SC-VAE-MI	λ	250, 500, 750
	h	0.25, 0.5, 0.75
SC-VAE-QD	λ	5, 10, 20, 50

D PARKINSON’S DATASET

D.1 IMPACT AND ANIMAL CARE STATEMENT

Phenotyping animal behavior is an early and essential step in drug discovery, and analyses of high-resolution 3D pose measurements provide a sensitive, reproducible, and scalable avenue for such preclinical assays. By releasing datasets and benchmarks for 3D pose analyses, we are supporting the continued development and acceleration of new phenotyping methods. We thus are facilitating the development of new therapeutics for neuropsychiatric disorders. All animal data were collected at AAALAC-accredited animal facilities. The care and experimental manipulation of all animals were reviewed and approved by university Institutional Animal Care and Use Committees.

D.2 LICENSES

Our datasets will be released under a CC BY 4.0 Attribution International license, which permits sharing and adapting the datasets without restrictions except for providing attribution to the dataset when used or adapted in a new medium.

D.3 ACCESS AND MAINTENANCE

Our datasets, train-test splits, Python code, and documentation for running all benchmarks will be made publicly available via our university library research data repository service. This service is designed to support long-term public access to research data and promote research transparency and reproducibility. The repository will provide stable and high-bandwidth access to the data, along with a minted digital object identifier (DOI) establishing a permanent record of the dataset’s release date. In addition, we will maintain a GitHub project page that links to this repository and provides a venue for interaction with the community.

D.4 ETHICS

Please see D.1 for a discussion of animal ethics. We acknowledge that by aiding the development of behavioral activity analysis approaches, bad actors could potentially use developed approaches for unethical purposes. However, we believe that the benefits behavioral analysis approaches offer for society, in terms of the potential to alleviate human disease burden, outweigh the (minimal) risks of misuse.

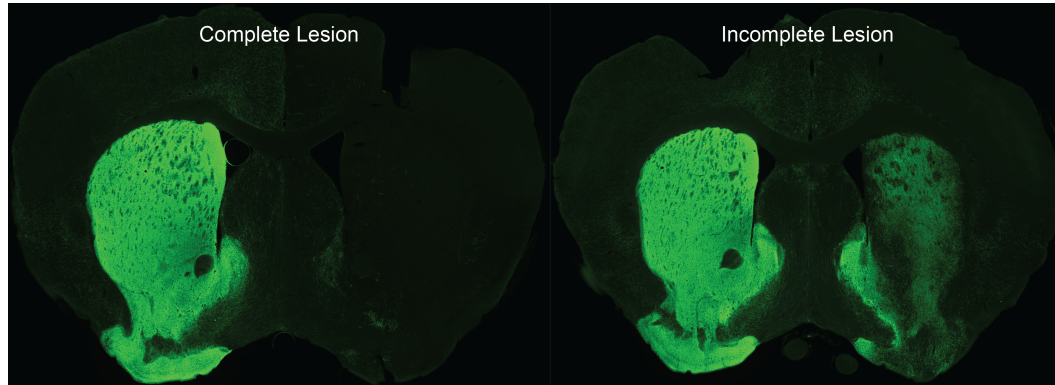


Figure 10: **Dopamine denervation in PD mouse brain.** Example fluorescent immunostaining in two mice after inducing Parkinson’s disease via 6-OHDA lesioning. Bright green indicates the presence of dopamine neurons. (left) Example complete lesion. (right) Example incomplete lesion.

D.5 DATASET COLLECTION

Adult *Drd1a-Cre* (8 females, 8 males, 18-20 weeks old) and *Adora2a-Cre* (10 females, 10 males, 18-20 weeks old) mice were anesthetized and implanted with a metal cannula (P1 tech) targeting the left medial forebrain bundle (-0.7mm AP, -1.2mm ML, -4.75mm DV). Custom-built headbars were then affixed to the skull using UV glue and dental cement.

After allowing 1 week for the mice to recover, mice were habituated to head fixation and to the open field (30cm x 30cm) arena, then a 1-hour baseline recording was performed in the arena another 1 week later. Immediately following the ‘baseline’ session, mice were head-fixed, and 0.9 μ L of a freshly made solution of 3.6mg/ml 6-OHDA and 1mg/ml ascorbic acid was infused through the cranial cannula at a rate of 0.1 μ L/min, allowing an additional 6 minutes for diffusion before removing the infusion cannula. 6-OHDA lesioned mice were provided with supportive care including daily subcutaneous saline injections and hand feeding with a mash made from a high-calorie diet supplement (Stat, ground-up macal) and ground up rodent feed (LabDiet 5001) until their weight stabilized. 2 weeks after the lesion, mice were again placed in the open-field arena for 1 hour to collect their ‘lesion’ behavioral data.

At the conclusion of the experiment, mice were deeply anesthetized with isoflurane and underwent a transcardial perfusion with 15 mL of 0.1M PBS followed by 50 mL of cold 4% PFA in 0.1M PBS, pH 7.4 for fixation. Brains were then dissected from the skull and soaked overnight at 4°C in the PFA solution, followed by 3 washes with 0.1M PBS. Each brain was then embedded in a mold in 5% agarose in order to collect 50 μ M coronal sections with a vibratome (Leica VT1200S) into wells containing 0.1M PBS.

The next day, brain sections were immunostained for tyrosine hydroxylase, a marker for dopamine neurons. Briefly, sections were washed in PBS before a 2-hour incubation in a blocking solution consisting of 5% goat serum, 3% bovine serum albumin, and 0.3% triton-x. Sections were then transferred to a half-block solution containing 1:1000 Rabbit α -TH (PeiFreez, P40101) overnight at 4°C with agitation. Sections were then washed in 0.1M PBS containing 0.1% tween before a 4-hour incubation in a half-block solution containing 1:1000 goat α -rabbit 488 (Invitrogen, A11008). Finally,

sections were washed in PBS containing tween, then PBS prior to mounting on glass slides (VWR) and coverslipping with Vectashield Vibrance with DAPI (Vector Labs).

Fluorescent images of each immunostained coronal section were then collected on a VS200 slide scanner. Analysis of pixel intensity of the fluorescent signal for TH was performed. For each brain, 4 sections were analyzed that evenly span the anterior to posterior axis of the striatum. On each section, the striatum was manually segmented in both hemispheres, and the fluorescent signal was summed across the sections for both the healthy and lesioned hemispheres. The value for the fluorescence in the lesioned hemisphere was then divided by the value for the fluorescence in the healthy hemisphere to yield the 'integrated fluorescence' for each animal.